

Complete methods set for scalable ion trap quantum information processing *

J. P. Home, D. Hanneke, J. D. Jost, J. M. Amini, D. Leibfried and D. J. Wineland.

*Time and Frequency Division,
National Institute of Standards and Technology,
Boulder,
CO 80305,
U.S.A.[†]*

(Dated: November 4, 2018)

Large-scale quantum information processors must be able to transport and maintain quantum information, and repeatedly perform logical operations. Here we demonstrate a combination of all the fundamental elements required to perform scalable quantum computing using qubits stored in the internal states of trapped atomic ions. We quantify the repeatability of a multi-qubit operation, observing no loss of performance despite qubit transport over macroscopic distances. Key to these results is the use of different pairs of $^9\text{Be}^+$ hyperfine states for robust qubit storage, readout and gates, and simultaneous trapping of $^{24}\text{Mg}^+$ “re-cooling” ions along with the qubit ions.

The long term goal for experimental quantum information processing is to realize a device involving large numbers of qubits and even larger numbers of logical operations [1, 2]. These resource requirements are defined both by the algorithms themselves, and the need for quantum error-correction, which makes use of many physical systems to store each qubit [1, 3]. The required components for building such a device are robust qubit storage, single and two-qubit logic gates, state initialization, readout, and the ability to transfer quantum information between spatially separated locations in the processor [2, 4, 5]. All of these components must be able to be performed repeatedly in order to realize a large scale device.

One experimental implementation of quantum information processing uses qubits stored in the internal states of trapped atomic ions. A universal set of quantum logic gates has been demonstrated using laser addressing [6, 7, 8], leading to a number of small-scale demonstrations of quantum information protocols including teleportation, dense-coding, and a single round of quantum error-correction [6]. A major challenge for this implementation is now to integrate scalable techniques required for large-scale processing.

A possible architecture for a large-scale trapped-ion device involves moving quantum information around the processor by moving the ions themselves, where the transport is controlled by time varying potentials applied to electrodes in a multiple-zone trap array [5, 9, 10]. The processor would consist of a large number of processing regions working in parallel, with other regions dedicated to qubit storage (memory). A general prescription for the required operations in a single processing region is the following (illustrated in Fig. 1), which includes all of the elements necessary for universal quantum computation [11]. (1) Two qubit ions are held in separate zones, allowing individual addressing for single qubit gates, state readout, or state initialization. (2) The ions are then combined in a single zone, and a two-qubit gate is performed. (3) The ions are separated, and one is moved to another region of the trap array. (4) A third ion is brought into this processing region from another part of the device. In this work we implement in a repeated fashion all of the steps which must be performed in a single processing region in order to realize this architecture.

* This manuscript has been accepted for publication in Science. This version has not undergone final editing. Please refer to the complete version of record at <http://www.sciencemag.org/>. The manuscript may not be reproduced or used in any manner that does not fall within the fair use provisions of the Copyright Act without the prior, written permission of AAAS.

Some elements of this architecture have been demonstrated in previous experiments [6, 12], which involved transport of ions in a multi-zone trap. However, these experiments did not involve the use of techniques required for building a large scale device, limiting the size of algorithms which could be performed. Primary limiting factors for these experiments were the loss of qubit coherence, caused by interaction with the fluctuating magnetic field environment, and motional excitation, which degrades the fidelity of subsequent two-qubit gates because of the finite wavelength of the gate control fields [13]. Motional excitation occurs as a result of imperfect control during transport and noisy electric fields emanating from the electrode surfaces [6]. In this work, we store qubits robustly using a pair of energy eigenstates in the ${}^9\text{Be}^+ 2s \text{ } ^2\text{S}_{1/2}$ hyperfine manifold (shown in Fig. 2) whose energy separation does not depend on the magnetic field to first order. For the ${}^9\text{Be}^+$ “qubit” ions used here, this condition is met at a magnetic field of 0.011964 T for the “memory” qubit states $|1\rangle \equiv |F=1, M_F=0\rangle$ and $|0\rangle \equiv |F=2, M_F=1\rangle$ (The states are labeled using the total angular momentum quantum numbers F and M_F). The insensitivity to magnetic field changes is crucial for preserving coherence in the presence of ambient temporal field fluctuations [14], and also greatly suppresses phase shifts caused by spatial variations in the average field experienced by an ion as it is transported throughout the multi-zone trap array. We remove motional excitation prior to each two-qubit gate by recooling “refrigerant” ${}^{24}\text{Mg}^+$ ions that are trapped along with the qubit ions. Laser cooling this second species sympathetically cools the first through the strong Coulomb interaction between the ions [15, 16, 17, 18].

A benchmark for scalability in this implementation is the repeated performance of a complete set of one and two-qubit logic gates combined with quantum information transport. We demonstrate repeatability of a unitary transformation \hat{U} which involves four single qubit gates, a two-qubit gate, and transport over $960 \mu\text{m}$ (the sequence for \hat{U} is shown in Fig. 3a). Ideally, \hat{U} implements the operation

$$\hat{U} = -\frac{e^{-i\pi/4}}{\sqrt{2}} \begin{pmatrix} -1 & 0 & 0 & i \\ 0 & 1 & i & 0 \\ 0 & i & 1 & 0 \\ i & 0 & 0 & -1 \end{pmatrix} \quad (1)$$

in the $|11\rangle, |10\rangle, |01\rangle, |00\rangle$ basis. We directly compare experimental implementation of \hat{U} and \hat{U}^2 using quantum process tomography [19]. Process tomography requires the process under investigation to be ap-

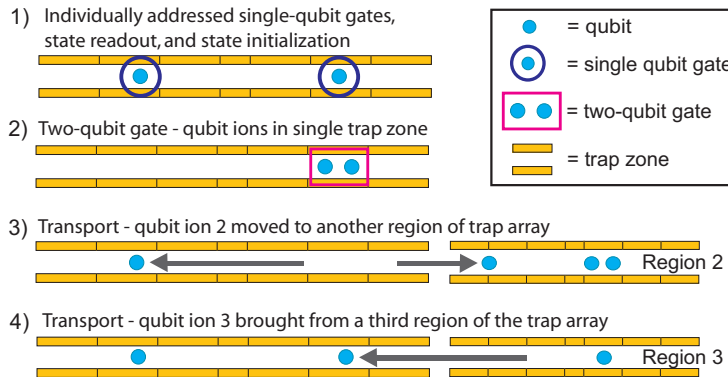


FIG. 1: Schematic of the sequence of operations implemented in a single processing region for building up a computation in the architecture of [5, 9]. A large-scale device would involve many of these processing regions performing operations in parallel, along with additional regions for memory. Generalized operations would use this block structure repeatedly, with perhaps some of the steps omitted.

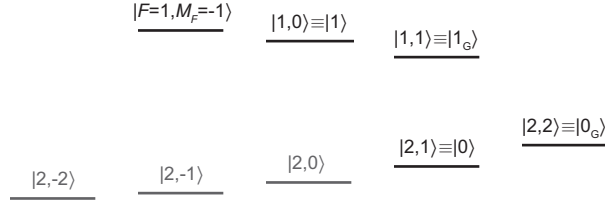


FIG. 2: Hybrid qubit storage in the ${}^9\text{Be}^+ 2s \, {}^2S_{1/2}$ hyperfine levels. The states are labeled using the total angular momentum quantum numbers F and M_F . $|1\rangle$, $|0\rangle$ are the qubit states used for single qubit gates and transport, and $|1_G\rangle$, $|0_G\rangle$ are used for two-qubit gates. For detection, the $|1, -1\rangle$ and $|2, 2\rangle$ states are used. At the applied magnetic field ($B \simeq 0.011964$ T), the frequencies for transitions between pairs of states with the same F are well resolved.

plied to sixteen input states, followed by measurement in nine orthogonal bases [20]. The input states are prepared using a combination of optical pumping and single-qubit operations, with the latter performed on each qubit individually. The analysis also requires individual single-qubit rotations, followed by individual state measurement of the qubits. The experiment therefore realizes all of the basic components illustrated in Fig. 1. We directly compare \hat{U} and \hat{U}^2 by running the experimental sequence for a given input/output combination on \hat{U} and \hat{U}^2 sequentially (shown in Fig. 3b), making the comparison of the two robust against long term drifts in experimental parameters. For each input/analysis combination, we repeat this sequence 350 times.

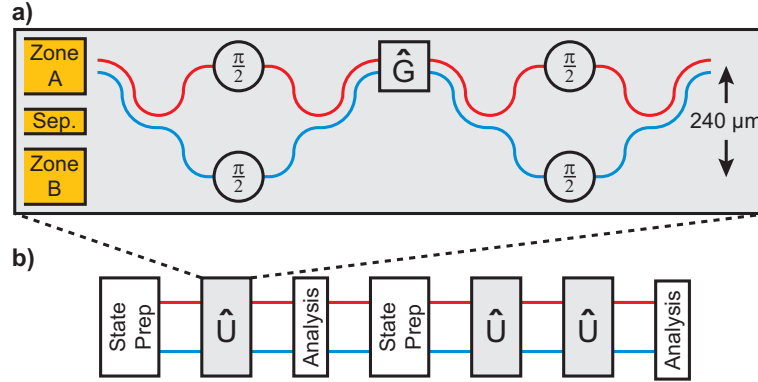


FIG. 3: a) Schematic of the qubit ion trajectories (solid red and dotted blue lines) and gate operations used to implement \hat{U} . The single qubit rotations are “ $\pi/2$ ” $\equiv R(\pi/2, 0)$ (eq. 2). The two-qubit gate implements $\hat{G} = D[(1, i, i, 1)]$. b) Full sequence used to perform process tomography on \hat{U} and \hat{U}^2 . This sequence is repeated 350 times for each setting of preparation/analysis.

The experiment utilizes two ${}^9\text{Be}^+$ and two ${}^{24}\text{Mg}^+$ ions, trapped in a six-zone linear Paul trap [12]. Each ${}^9\text{Be}^+$ ion is used to store one qubit, and is accompanied at all times by a ${}^{24}\text{Mg}^+$ refrigerant ion, which is used for sympathetic cooling. The ion order is initialized to ${}^9\text{Be}^+ - {}^{24}\text{Mg}^+ - {}^{24}\text{Mg}^+ - {}^9\text{Be}^+$ at the start of the experimental sequence, and remains in this order throughout [21].

Coherent manipulations of the internal and motional states of the ions are performed using laser-induced stimulated Raman transitions [9]. Single qubit gates are implemented in the basis $|1\rangle$, $|0\rangle$ by

resonant Rabi flopping, applying the rotation

$$R(\theta, \phi) = \begin{pmatrix} \cos(\theta/2) & -ie^{-i\phi} \sin(\theta/2) \\ -ie^{i\phi} \sin(\theta/2) & \cos(\theta/2) \end{pmatrix}, \quad (2)$$

where θ is proportional to the Raman pulse duration and ϕ is chosen by adjusting the relative phase of the Raman light fields at the ion. We individually address the two qubit ions by holding them in two trap zones 240 μm apart, and switching the laser beams between zones.

To implement two-qubit gates, we first combine all of the ions into a single zone. The four-ion linear chain exhibits four axial vibrational normal modes caused by the Coulomb coupling between ions [21]. After recombination, these modes contain significant excess energy, mainly caused by imperfect control of the potentials used during separation and recombination. Therefore, prior to each two-qubit gate, we cool each mode to near the quantum ground state ($\langle n \rangle \sim 0.06$) using a combination of Doppler cooling and resolved sideband cooling on the $^{24}\text{Mg}^+$ ions [15, 22]. Importantly, the cooling light only interacts with $^{24}\text{Mg}^+$, leaving the qubits stored in $^9\text{Be}^+$ intact [15].

The composite two-qubit gate makes use of a geometric phase gate [7] to implement $\hat{G} = D[(1, i, i, 1)]$, where $D[\underline{v}]$ is a diagonal matrix with the vector \underline{v} on the diagonal. The phase acquired by the $|10\rangle$ and $|01\rangle$ states is obtained by transient simultaneous excitation of the two highest-frequency normal modes by use of a state-dependent optical dipole force [22]. The state dependence of this force is derived from a differential light shift between the two qubit states, which is highly suppressed for field-independent transitions [14, 23]. We thus use a hybrid scheme for qubit storage, mapping the qubits into a different state manifold for the two-qubit gate [22, 24, 25]. Prior to applying the optical dipole force, we transfer each qubit into a pair of states with a sizeable differential light shift – the “gate” manifold $|1_G\rangle \equiv |1, 1\rangle$, $|0_G\rangle \equiv |2, 2\rangle$ (Fig. 2). After applying the state-dependent force, we reverse this transfer and the ions are again separated [22]. The gate manifold is sensitive to magnetic field fluctuations, which can lead to qubit dephasing. We suppress these effects using spin-echo techniques [21].

We employ quantum process tomography to characterize our implementation of the unitary operation \hat{U} , including any experimental imperfections [19, 20]. The evolution of the qubit system (including that caused by undesired interactions with the environment) is described by a completely positive linear map $\rho_{\text{out}} = \mathcal{E}_{\hat{U}}(\rho_{\text{in}})$ [19] on the input density matrix $\rho_{\text{in}} = \sum_{i,j} c_{i,j} |i\rangle \langle j|$, where the $c_{i,j}$ are complex numbers and i, j are labels that each run over the eigenstates $|11\rangle, |10\rangle, |01\rangle, |00\rangle$. Following [26], we represent the map by a 16×16 matrix

$$E_{\hat{U}} = \sum_{i,j} |i\rangle \langle j| \otimes \mathcal{E}_{\hat{U}}(|i\rangle \langle j|). \quad (3)$$

In order to extract this process matrix, we experimentally apply the process to 16 input states made up of tensor products of the states $|1\rangle, |0\rangle, (|0\rangle - |1\rangle)/\sqrt{2}$ and $(|0\rangle + i|1\rangle)/\sqrt{2}$. For each output density matrix, we apply nine sets of rotations, which allow us to measure the expectation values of the operators $\sigma_s \otimes \sigma_t$, where the $\sigma_{s,t}$ run over the Pauli matrices $I, \sigma_x, \sigma_y, \sigma_z$. Our state readout performs a projective measurement in the Z basis on each ion independently. We first transfer population from $|0\rangle$ to $|2, 2\rangle$, and from $|1\rangle$ to $|1, -1\rangle$, and subsequently drive the cycling transition $2s \ ^2S_{1/2} |2, 2\rangle \leftrightarrow 2p \ ^2P_{3/2} |3, 3\rangle$ for 200 μs , where $|2, 2\rangle$ strongly fluoresces and $|1, -1\rangle$ does not [22]. We collect a small fraction of the emitted photons on a photomultiplier tube. We run the sequence shown in Fig. 3b 350 times for each of the 16 input states and nine measurement rotations. The process matrix is obtained directly from the recorded photon counts and measurement/preparation settings using a maximum-likelihood method that ensures that the reconstructed process matrix is physical [26].

Experimentally obtained process matrices for one and two applications of \hat{U} are shown in Fig. 4. From the reconstructions, we can calculate various measures of the fidelity with which the processes

were implemented. A direct comparison between experimental results and the ideal case is given by the entanglement fidelity $F \equiv \text{Tr}(E_{\text{ideal}}E)/16$ [27]. We find $F_{\hat{U}} = 0.922(4)$ for a single application of \hat{U} , and $F_{\hat{U}^2} = 0.853(5)$ for two applications (error estimates are the standard error on the mean obtained from parametric bootstrap resampling [22]). As an additional measure of operation fidelity, we take the mean \bar{f} of the fidelity $f(\rho_{\text{ideal}}, \rho_E) \equiv [\text{Tr}(\sqrt{\sqrt{\rho_{\text{ideal}}}\rho_E\sqrt{\rho_{\text{ideal}}}})]^2$ [28] between the output density matrices obtained from the ideal and experimental processes for an unbiased set of 36 input states (formed from the eigenstates of $\sigma_s \otimes \sigma_t$, where $\sigma_{s,t}$ run over $\sigma_x, \sigma_y, \sigma_z$). We obtain a mean state fidelity of $\bar{f}_{\hat{U}} = 0.940(4)$ for $E_{\hat{U}}$ and $\bar{f}_{\hat{U}^2} = 0.890(4)$ for $E_{\hat{U}^2}$. We can compare these values to the entanglement fidelities using the relation $\bar{f} = (4F + 1)/5$ [27], and see that they are consistent.

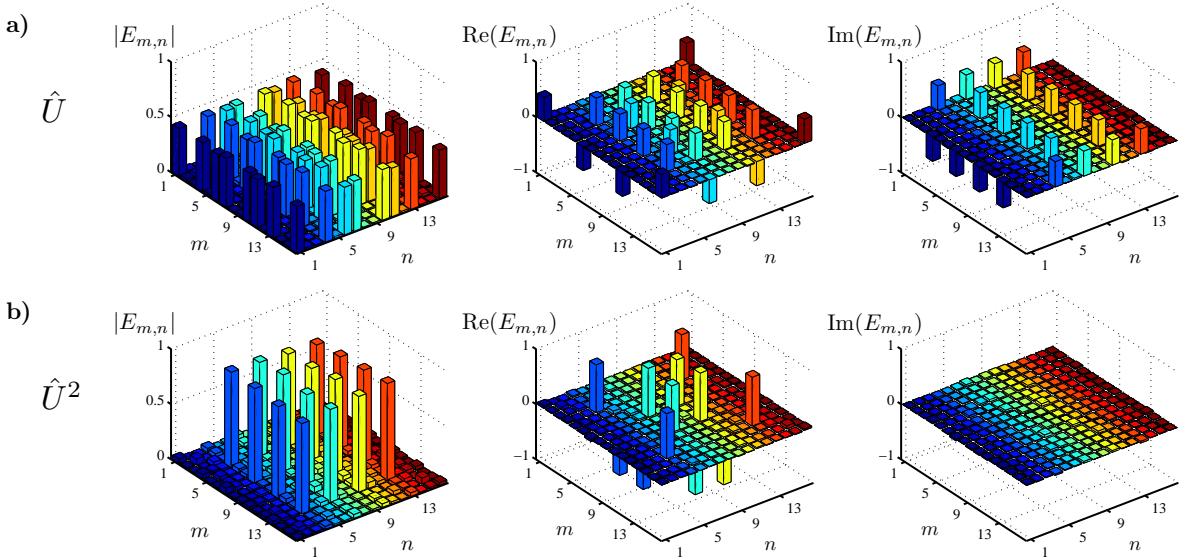


FIG. 4: Reconstructed process matrix for a) \hat{U} and b) two repetitions of \hat{U} . The map $\mathcal{E}(|i\rangle\langle j|)$ produces a matrix $\mathcal{E}_{k,l}$ for each element $|i\rangle\langle j|$. Hence elements of the matrix E are labeled by $m = 4(i-1) + k, n = 4(j-1) + l$, where the factor 4 results from the size of the two-qubit state space. For example, the $|11\rangle\langle 00|$ ($i = 1, j = 4$) element of an input density matrix is mapped to $\mathcal{E}(|11\rangle\langle 00|)$, a 4×4 block of E given by $m \in [1, 4]$ and $n \in [13, 16]$. The position of each peak is in agreement with the theoretical prediction.

To compare the performance of a second application of \hat{U} relative to the first, we can compare its experimental repetition $\mathcal{E}_{\hat{U}^2}(\rho_{\text{in}})$ to a numeric repetition of the experimental map $\mathcal{E}_{\hat{U}}(\rho_{\text{in}})$, i.e., to $\mathcal{E}_{\hat{U}\hat{U}}(\rho_{\text{in}}) \equiv \mathcal{E}_{\hat{U}}(\mathcal{E}_{\hat{U}}(\rho_{\text{in}}))$. Evaluating the fidelities for each against the ideal case yields $F_{\hat{U}^2}/F_{\hat{U}\hat{U}} = 1.003(13)$ and $\bar{f}_{\hat{U}^2}/\bar{f}_{\hat{U}\hat{U}} = 1.004(10)$, indicating that the operation fidelity is the same for each application of \hat{U} . We can also make a direct comparison between the processes performed by our implementation of \hat{U} and \hat{U}^2 by taking the mean fidelity between $\rho_{\hat{U}\hat{U}} = \mathcal{E}_{\hat{U}}(\mathcal{E}_{\hat{U}}(\rho_{\text{in}}))$ and $\rho_{\hat{U}^2} = \mathcal{E}_{\hat{U}^2}(\rho_{\text{in}})$ for the 36 input states. We find $\bar{f}(\rho_{\hat{U}\hat{U}}, \rho_{\hat{U}^2}) = 0.987(3)$. Although this number is not unity, as might be expected, the deviation can be

ascribed to bias in the maximum-likelihood reconstruction method for finite sample size [22]. Our results are thus consistent with the same operation being performed by the experiment for each application of \hat{U} .

Sources of error in our system arise primarily from spontaneous photon scattering ($\sim 1.5\%$ per \hat{U}) [29] and intensity fluctuations of the Raman light fields at the percent level. In order to characterize the loss of fidelity caused by single-qubit rotations, we apply process tomography to the experimental sequence, but without the state-dependent force pulses. In this case the ions are always in a product state and the process matrix for each can be obtained independently. The resulting process matrices have mean state fidelity relative to the ideal case of 0.97 for a single run of the sequence (which uses eight rotations per ion including qubit manifold transfer and spin-echo pulses). During the two-qubit gate, the spin states are entangled with the motion. From separate measurements of motional coherence, we estimate the infidelity from this source to be less than 1×10^{-3} .

Many challenges remain before large-scale ion trap quantum information processing becomes a reality, including increasing fidelities to those required for fault-tolerant quantum error correction [1, 3], and meeting the considerable technical challenge of controlling ions in large multi-dimensional trap arrays [10]. Both of these challenges could potentially contain problems which have not been considered here, and which may require combining our approach with alternative methods, for instance entanglement distribution using photonic networks [30]. Nevertheless, the combination of techniques demonstrated here includes all of the basic building blocks required in this architecture, and opens up new possibilities for quantum information processing as well as state and process engineering.

This work was supported by IARPA and the NIST Quantum Information Program. J. P. H. acknowledges support from a Lindemann Trust Fellowship. We thank E. Knill for helpful discussions, J. J. Bollinger for technical assistance and Y. Colombe for comments on the manuscript. This paper is a contribution by the National Institute of Standards and Technology and not subject to U.S. copyright.

[†] Electronic address: jonathan.home@gmail.com

- [1] E. Knill, *Nature* **434**, 39 (2005).
- [2] A. M. Steane, *Quant. Inf. and Comp.* **7**, 171 (2007).
- [3] A. M. Steane, *Phys. Rev. A* **68**, 042322 (2003).
- [4] D. P. DiVincenzo, *Fortschr. Phys.* **48**, 771 (2000).
- [5] D. Kielpinski, C. Monroe, and D. J. Wineland, *Nature* **417**, 709 (2002).
- [6] R. Blatt and D. J. Wineland, *Nature* **453**, 1008 (2008).
- [7] D. Leibfried, B. DeMarco, V. Meyer, D. Lucas, M. Barrett, J. Britton, W. M. Itano, B. Jelenkovic, C. Langer, T. Rosenband, et al., *Nature* **422**, 412 (2003).
- [8] J. Benhelm, G. Kirchmair, C. F. Roos, and R. Blatt, *Nature Phys.* **4**, 463 (2008).
- [9] D. J. Wineland, C. Monroe, W. M. Itano, D. Leibfried, B. E. King, and D. M. Meekhof, *J. Res. Nat. Inst. Stand. Technol.* **103**, 259 (1998).
- [10] R. B. Blakestad, C. Ospelkaus, A. P. VanDevender, J. M. Amini, J. Britton, D. Leibfried, and D. J. Wineland, *Phys. Rev. Lett.* **102**, 153002 (2009).
- [11] A. Barenco, C. Bennett, R. Cleve, D. D. N. Margolus, P. Shor, T. Sleator, J. Smolin, and H. Weinfurter, *Phys. Rev. A* **52**, 3457 (1995).
- [12] M. D. Barrett, J. Chiaverini, T. Schaetz, J. Britton, W. M. Itano, J. D. Jost, E. Knill, C. Langer, D. Leibfried, R. Ozeri, et al., *Nature* **429**, 737 (2004).
- [13] A. Sørensen and K. Mølmer, *Phys. Rev. A* **62**, 022311 (2000).
- [14] C. Langer, R. Ozeri, J. Jost, J. Chiaverini, B. DeMarco, A. Ben-Kish, R. Blakestad, J. Britton, D. Hume, W. Itano, et al., *Phys. Rev. Lett.* **95**, 060502 (2005).
- [15] M. D. Barrett, B. DeMarco, T. Schaetz, D. Leibfried, J. Britton, J. Chiaverini, W. M. Itano, B. Jelenkovic, J. D. Jost, C. Langer, et al., *Phys. Rev. A* **68**, 042302 (2003).

- [16] H. Rohde, S. T. Gulde, C. F. Roos, P. A. Barton, D. Leibfried, J. Eschner, F. Schmidt-Kaler, and R. Blatt, J. Opt. B: Quantum Semiclass. Opt. **3**, S34 (2001).
- [17] B. B. Blinov, L. Deslauriers, P. Lee, M. J. Madsen, R. Miller, and C. Monroe, Phys. Rev. A **65**, 040304(R) (2002).
- [18] J. P. Home, M. J. McDonnell, D. J. Szwer, B. C. Keitch, D. M. Lucas, and A. M. Steane, Phys. Rev. A **79**, 050305(R) (2009).
- [19] M. A. Nielsen and I. L. Chuang, *Quantum Computation and Quantum Information* (Cambridge University Press, Cambridge, 2000).
- [20] M. Riebe, K. Kim, P. Schindler, T. Monz, P. O. Schmidt, T. K. Körber, W. Hänsel, H. Häffner, C. F. Roos, and R. Blatt, Phys. Rev. Lett. **97**, 220407 (2006).
- [21] J. D. Jost, J. P. Home, J. M. Amini, D. Hanneke, R. Ozeri, C. Langer, J. J. Bollinger, D. Leibfried, and D. J. Wineland, Nature **459**, arXiv:0901.4779 (2009).
- [22] Materials and methods are available as supporting material on *Science* Online.
- [23] P. J. Lee, K.-A. Brickman, L. Deslauriers, P. C. Haljan, L. M. Duan, and C. Monroe, J. Opt. B: Quantum Semiclass. Opt. **7**, S371 (2005).
- [24] N. Lundblad, J. M. . Obrecht, I. B. Spielman, and J. V. Porto, arXiv:0902.3213 (2009).
- [25] G. Kirchmair, J. Benhelm, F. Zähringer, R. Gerritsma, C. F. Roos, and R. Blatt, Phys. Rev. A. **79**, 020304 (2009).
- [26] Z. Hradil, J. Řeháček, J. Fiurášek, and M. Ježek, *Quantum State Estimation* (Springer-Verlag, 2004), chap. Maximum-Likelihood Methods in Quantum Mechanics, pp. 59–112.
- [27] M. Horodecki, P. Horodecki, and R. Horodecki, Phys. Rev. A **60**, 1888 (1999).
- [28] R. Jozsa, J. Mod. Opt. **41**, 2315 (1994).
- [29] R. Ozeri, W. M. Itano, R. B. Blakestad, J. Britton, J. Chiaverini, J. D. Jost, C. Langer, D. Leibfried, R. Reichle, S. Seidelin, et al., Phys. Rev. A. **75**, 042329 (2007).
- [30] D. L. Moehring, P. Maunz, S. Olmschenk, K. C. Younge, D. N. Matsukevich, L.-M. Duan, and C. Monroe, Nature **449**, 68 (2007).
- [31] B. Efron and R. J. Tibshirani, *An Introduction to the Bootstrap* (Chapman & Hall, 1993).

Materials and Methods

The Supporting Online Materials provide further details about the sympathetic cooling, the use of state-dependent forces to implement a geometric phase gate using multiple motional modes, transfer between the gate and memory qubit manifolds, state detection and error analysis for quantum process tomography.

Sympathetic cooling.

After recombining the ions in a single trap zone, each of the axial modes of the four ion ${}^9\text{Be}^+ - {}^{24}\text{Mg}^+ - {}^{24}\text{Mg}^+ - {}^9\text{Be}^+$ chain contains significant excess energy. The precise amount is difficult to characterize, since the distribution of population in the Fock state basis is not well known. For the experiments presented here, we require three stages of cooling to attain the ground state. We start with Doppler cooling, which thermalizes the state with a mean vibrational occupation number $\bar{n} \sim 15$. We then use cycles of resolved sideband cooling on both the second and first sidebands of each motional mode to prepare the ground state with a fidelity of ~ 0.94 for each mode. In total, the cooling takes 5.1 ms per \hat{U} , and this is the limiting factor in the operation time (followed by transport/separation, which takes 3.6 ms per \hat{U}). The motional excitation produced in our experiment is much higher than in similar previous work [12], which we attribute primarily to use of voltage supplies with an voltage update rate below the typical trap frequencies [10]. In future this time should be able to be substantially reduced by using supplies with an increased update rate.

Two-qubit logic gate.

The two-qubit gate follows the basic method used in [7], with the modification that we simultaneously excite two motional modes rather than one. This speeds up the gate for a given laser intensity, and thus reduces the error due to spontaneous photon scattering. We perform the gate with the ions in the spatial configuration ${}^9\text{Be}^+ - {}^{24}\text{Mg}^+ - {}^{24}\text{Mg}^+ - {}^9\text{Be}^+$. The two modes we excite are the highest frequency axial modes, which are separated in frequency by $2\pi \times 251$ kHz [21]. The difference frequency of the two Raman light fields that generate the state-dependent force is $\omega = \omega_3 + \delta = \omega_4 - 2\delta$, where ω_3, ω_4 are the frequencies of the motional modes, and $\delta = 2\pi \times 83.6$ kHz. The state-dependent force is applied for a duration $t_G = 2\pi/\delta$, ensuring that the spin states are disentangled from both motional modes at the end of the pulse [7]. We choose the axial confinement such that the two ${}^9\text{Be}^+$ ions are separated by a half-integer number of wavelengths of the optical dipole potential. The oscillation of the two ${}^9\text{Be}^+$ ions in the ω_4 mode is out of phase, resulting in motional excitation of this mode for $|0_G 1_G\rangle$ and $|1_G 0_G\rangle$. For the ω_3 mode, motion is excited (and thus phase acquired) for all qubit states. This can lead to unwanted $\hat{\sigma}_z$ rotations being implemented along with the phase gate. For this reason, and to increase robustness against other sources of error (such as Stark shifts) during the motional excitation, we apply the phase gate in two pulses, with a $R(\pi, \phi_G)$ pulse on $|0_G\rangle \leftrightarrow |1_G\rangle$ applied between the two. This is followed by a second $R(\theta, \phi'_G)$ pulse (see next section). The ratio of contributions to the gate phase due to each mode is $\Phi_3/\Phi_4 = 2.72$.

Transfer between the gate and memory qubit manifolds

In order to implement the state-dependent optical dipole force, we transfer from the field-independent manifold $|1\rangle, |0\rangle$ to the “gate” manifold $|1_G\rangle, |0_G\rangle$. This is performed by applying $R(\pi, \phi)$ to $|1\rangle \leftrightarrow |1_G\rangle$ and $|0\rangle \leftrightarrow |0_G\rangle$ sequentially (for these and other transitions described in this section, the rotation basis is given by $(|h\rangle, |l\rangle)$, where h (l) indicates the higher (lower) energy state). Each of these pulses imprints a different phase ϕ_1, ϕ_0 on the qubit state. After the state-dependent force pulses have been applied, we repeat this transfer in reverse order, taking the qubit back into the $|1\rangle, |0\rangle$ manifold and imprinting phase ϕ'_1, ϕ'_0 . While in the gate manifold, we apply two spin-echo pulses $R(\pi, \phi_G), R(\pi, \phi'_G)$ on $|1_G\rangle \leftrightarrow |0_G\rangle$. As a result the final phase imprinted on the qubit by these rotations depends on the phase differences $\phi_1 - \phi'_1, \phi_0 - \phi'_0$ and $\phi_G - \phi'_G$. If each transition is driven with independent oscillators these phase differences are zero. In our case these are non-zero due to the use of tunable frequency sources for driving Raman transitions, and we adjust the phase of all subsequent single-qubit gates to compensate for this.

Detection.

The state of each ion is read out individually. Due to the lack of multiple detection apparatus, we perform state readout sequentially. First, with the ions in separate zones, we transfer population from the qubit memory levels into the qubit readout levels $|2, 2\rangle$ and $|1, -1\rangle$, using a sequence of $R(\pi, 0)$ pulses on $|2, 1\rangle \rightarrow |2, 2\rangle$ and $|1, 0\rangle \rightarrow |1, -1\rangle$. We then resonantly drive the cycling transition $2s\ {}^2S_{1/2} |2, 2\rangle \leftrightarrow 3p\ {}^2P_{3/2} |3, 3\rangle$ for the ion in trap zone A (ion 1) and detect. For an ion in $|2, 2\rangle$, the distribution of the number of photons collected in the $200\ \mu\text{s}$ detection period closely approximates a Poisson distribution with mean 10 counts. For an ion in $|1, -1\rangle$, the distribution has two components, the dominant contribution coming from background scatter of the laser light (which has a Poisson distribution with mean 0.4 counts),

and a much smaller exponential contribution due to repumping of the $|1, -1\rangle$ state into $|2, 2\rangle$ over the detection period (the repumping probability is $\approx 1 \times 10^{-3}$ over $200 \mu\text{s}$). In order to detect the second ion, we recombine the ions in zone A, and again drive the cycling transition. To ensure that ion 1 contributes negligibly to the second detection, prior to recombination we transfer all population in this ion to $|1, -1\rangle$ by optical pumping to $|2, 2\rangle$ followed by $R(\pi, 0)$ transfer pulses on $|2, 2\rangle \rightarrow |1, 1\rangle$, $|1, 1\rangle \rightarrow |1, 0\rangle$, $|1, 0\rangle \rightarrow |1, -1\rangle$. If the first of these was imperfect, it might leave population in the fluorescing state, hence we perform a transfer pulse from $|2, 2\rangle \rightarrow |2, 1\rangle$ to protect against this ($|2, 1\rangle$ scatters relatively few photons for our detection parameters).

Tomography error analysis by resampling.

Statistical errors for values given in the text are derived from parametric bootstrap resampling [31]. Using the process matrix obtained from the experimental data, we generated 100 sample data sets. This was performed using a random number generator combined with the known probability distributions for the photon counts, and choosing from a normal distribution of Rabi frequencies consistent with observed intensity fluctuations for the rotation angles θ used for preparation/analysis rotations. For each sample data set, we obtained a process matrix, and evaluated the relevant fidelities. The quoted statistical error estimates are the standard error on the mean obtained from the distributions of results. These distributions are centred about one standard error below the value obtained directly from the experimental data. This shift is due to the fact that the maximum-likelihood estimation is only an unbiased estimator in the limit of infinite sample size, and that the estimation constrains the solution to lie within the set of physically allowed process matrices. This implies that the quoted experimental fidelities are underestimates.

The effect of reconstruction bias is illustrated by the following example. We numerically generated 100 sample data sets using both the experimentally obtained $\mathcal{E}_{\hat{U}}(\rho)$ and the application of this same map twice $\mathcal{E}_{\hat{U}}(\mathcal{E}_{\hat{U}}(\rho))$. For each data set, we performed the maximum likelihood analysis, obtaining $E'_{\hat{U}}$ and $E'_{\hat{U}^2}$. We compared the performance of these two processes by taking the mean fidelity between $\rho'_{\hat{U}\hat{U}} = \mathcal{E}'_{\hat{U}}(\mathcal{E}'_{\hat{U}}(\rho))$ and $\rho'_{\hat{U}^2} = \mathcal{E}'_{\hat{U}^2}(\rho)$ over the set of 36 input states. The average value of this fidelity over the 100 sample data sets was 0.989(2), where for unbiased reconstruction this value would be one. This means that the experimental value of 0.987(3) is consistent with the gate operation being the same for each repetition.